Provided for non-commercial research and education use.
Not for reproduction, distribution or commercial use.

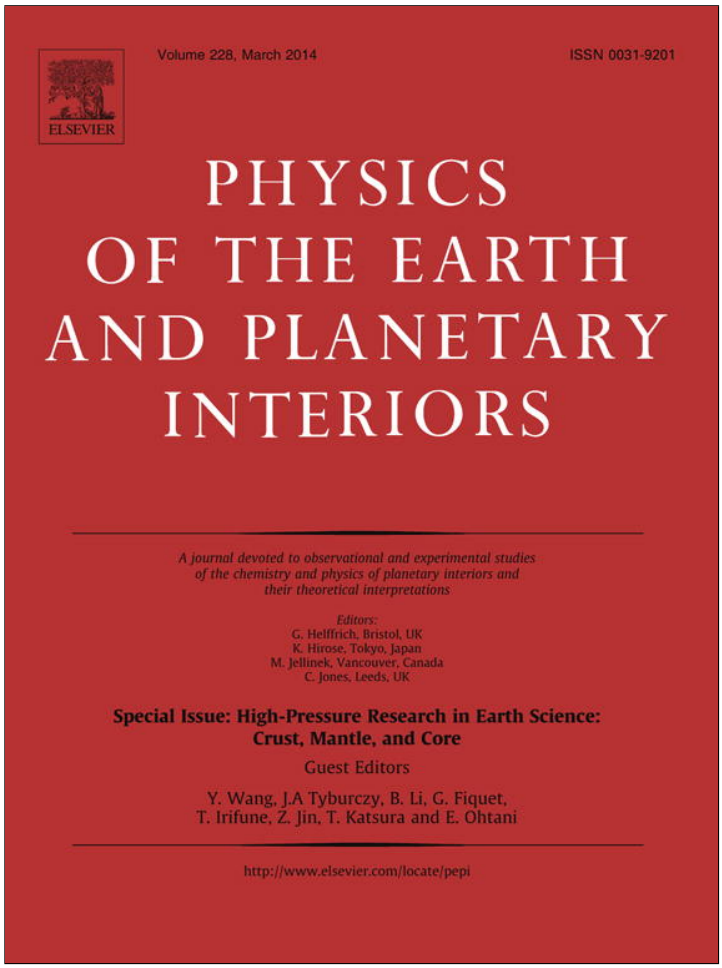


This article appeared in a journal published by Elsevier. The attached copy is furnished to the author for internal non-commercial research and education use, including for instruction at the authors institution and sharing with colleagues.

Other uses, including reproduction and distribution, or selling or licensing copies, or posting to personal, institutional or third party websites are prohibited.

In most cases authors are permitted to post their version of the article (e.g. in Word or Tex form) to their personal website or institutional repository. Authors requiring further information regarding Elsevier's archiving and manuscript policies are encouraged to visit:

http://www.elsevier.com/authorsrights

Author's personal copy

Physics of the Earth and Planetary Interiors 228 (2014) 269–280

Contents lists available at ScienceDirect

Physics of the Earth and Planetary Interiors

journal homepage: www.elsevier.com/locate/pepi

# Toward comprehensive studies of liquids at high pressures and high temperatures: Combined structure, elastic wave velocity, and viscosity measurements in the Paris–Edinburgh cell

Yoshio Kono [a,*], Changyong Park [a], Curtis Kenney-Benson [a], Guoyin Shen [a], Yanbin Wang [b]

[a] HPCAT, Geophysical Laboratory, Carnegie Institution of Washington, 9700 S. Cass Avenue, Argonne, IL 60439, United States
[b] GeoSoilEnviroCARS, Center for Advanced Radiation Sources, The University of Chicago, 5640 S. Ellis Avenue, Chicago, IL 60637, United States

ARTICLE INFO

*Article history:*
Available online 18 September 2013
Edited by M. Jellinek

*Keywords:*
Liquid
Liquid structure
Elastic wave velocity
Viscosity
High pressure

ABSTRACT

Techniques for measuring liquid structure, elastic wave velocity, and viscosity under high pressure have been integrated using a Paris–Edinburgh cell at Beamline 16-BM-B, HPCAT of the Advanced Photon Source. The Paris–Edinburgh press allows for compressing large volume samples (up to 2 mm in both diameter and length) up to ~7 GPa and 2000 °C. Multi-angle energy dispersive X-ray diffraction provides structure factors of liquid to a large Q of ~19 Å. Ultrasonic techniques have been developed to investigate elastic wave velocity of liquids combined with the X-ray imaging. Falling sphere viscometry, using high-speed X-ray radiography (>1000 frames/s), enables us to investigate a wide range of viscosity, from those of high viscosity silicates or oxides melts to low viscosity (<1 mPa s) liquids and fluids such as liquid metals or salts. The integration of these multiple techniques has promoted comprehensive studies of structure and physical properties of liquids as well as amorphous materials at high pressures and high temperatures, making it possible to investigate correlations between structure and physical properties of liquids *in situ*.

© 2013 Elsevier B.V. All rights reserved.

## 1. Introduction

Knowledge on the structure and physical properties of liquids at high pressures and high temperatures is important in understanding dynamics and evolution of the interiors of the Earth and other planets. In materials science, liquid materials possess many properties that are distinct from solids, with unique applications to industrial and engineering. However, understanding the physics of liquid materials remains a challenge, especially under high pressure. Structure and physical properties of liquids have been much less studied than those of crystalline materials due to experimental difficulties. Some efforts have been made to investigate structure of liquids (e.g., Tsuji et al., 1989; Mezouar et al., 2002; Shen et al., 2004; Yamada et al., 2011), physical properties such as density (e.g., Katayama et al., 1998; Shen et al., 2002; Ohtani et al., 2005), viscosity (e.g., Kushiro et al., 1976; Kanzaki et al., 1987; Dobson et al., 2000; Terasaki et al., 2001; Perrillat et al., 2010), and elastic wave velocity (e.g., Krisch et al., 2002; Decremps et al., 2009; Nishida et al., 2013). However, these results were often based on individual techniques, and the discussions were made by comparisons with results obtained by other researchers using in different apparatus using different techniques. Integration of these techniques should promote a more comprehensive understanding of the behavior of liquids at high pressures and high temperatures. In this paper, we report a new experimental setup which integrates liquid structure, elastic wave velocity, and viscosity measurements in a Paris–Edinburgh cell at high pressures and high temperatures at Beamline 16-BM-B, HPCAT, the Advanced Photon Source (APS).

## 2. Beamline overview

Fig. 1 shows the experimental setup in the 16-BM-B experimental station, which is capable of white beam X-ray diffraction and radiography experiments using a Paris–Edinburgh (PE) cell. The PE cell allows compression of large sample volumes (up to 2 mm in both diameter and length) at high pressures and high temperatures. Liquid structure studies are conducted by the multi-angle energy-dispersive X-ray diffraction (EDXD) technique. A large Huber stage holding a Ge solid state detector (Ge-SSD) allows precise control $2\theta$ angle from 2° to 39.5°. Elastic wave velocities can be determined *in situ* by measuring both elastic wave travel times using ultrasonic techniques and sample length using white X-ray radiography. For sample length measurement, a CCD camera (Prosilica GC1380) was used. The camera can be moved in and out of the beam vertically to avoid interference with the collimator for X-ray diffraction measurement. Another camera, a high-speed Photron SA3, is located at the downstream side of the Ge-SSD. The SA3

* Corresponding author. Tel.: +1 630 252 4078.
*E-mail address:* ykono@ciw.edu (Y. Kono).

0031-9201/$ - see front matter © 2013 Elsevier B.V. All rights reserved.
http://dx.doi.org/10.1016/j.pepi.2013.09.006

Author's personal copy



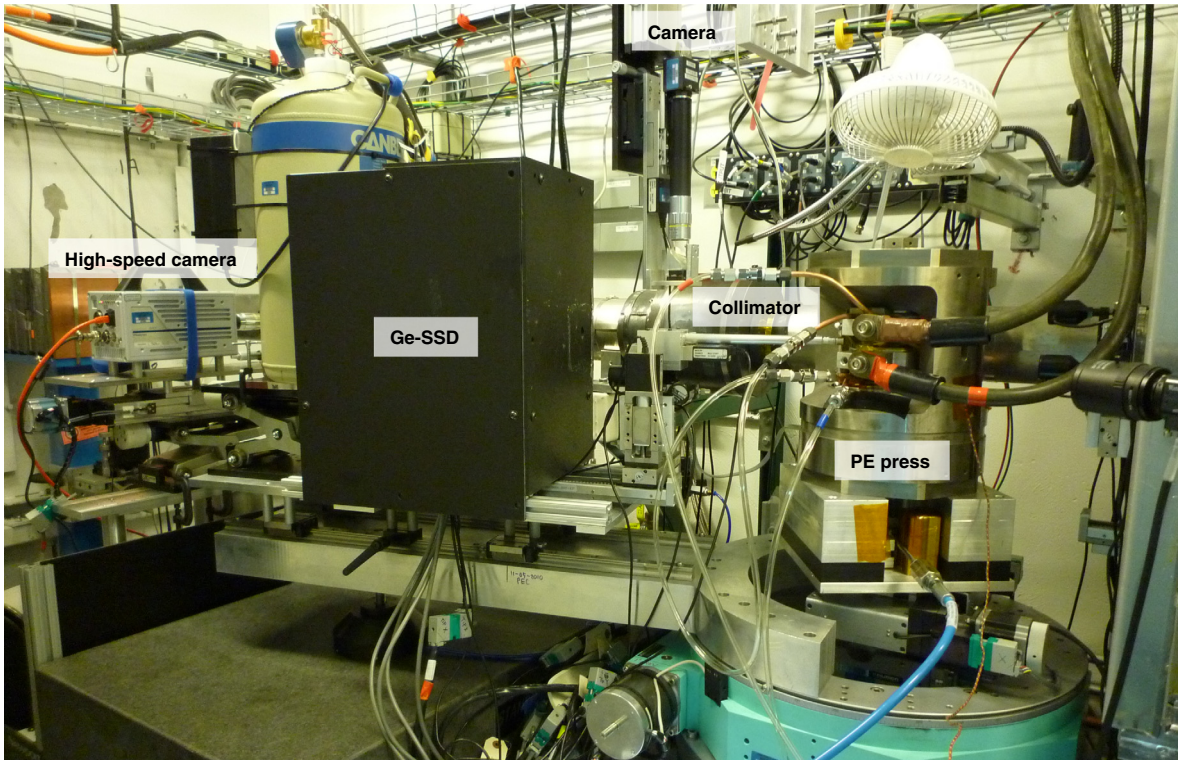


**Fig. 1.** A photograph of the experimental setup at the sector 16-BM-B, HPCAT.

has a high frame rate of >1000 frames/s (fps) and is used for high-speed falling sphere viscosity measurement.

## 3. High-pressure and high-temperature experiments in the Paris–Edinburgh cell

High-pressure experiments are conducted with a VX-3 Paris–Edinburgh press (Besson et al., 1992; Klotz et al., 2004). Cup-shaped WC anvils with the cup diameter of 12 mm and the bottom diameter of 3 mm are used to generate high pressures (Yamada et al., 2011). Fig. 2 shows a standard cell assembly design for liquid structure measurement and/or viscosity measurement. We use a different design of cell assembly for ultrasonic measurement (see Section 5 below). The cell assembly mainly consists of boron–epoxy (BE) gaskets, an MgO ring, $ZrO_2$ caps, a graphite heater, and a BN capsule. Capsule material differs depending on sample. For example, graphite inner capsule was used for silicate melt experiments inside BN sleeve (Yamada et al., 2011; Sakamaki et al., 2012). Large volume samples of up to 2 mm in both diameter and length are available in this cell assembly. However, the height of X-ray window is limited by the anvil gap at high pressures. At around 7 GPa and 1700 °C, a typical anvil gap is ~0.7 mm.

A ring-shaped BE (boron:epoxy = 4:1 in weight ratio) is used as gasket with a supporting outer polycarbonate plastic (Lexan) ring. The BE gasket and $ZrO_2$ caps in the assembly provide good thermal insulation for high temperature experiments. An MgO ring is placed between BE gasket and graphite heater to increase stability of the cell assembly and maintain anvil gap. High temperature is generated by the graphite heater. Fig. 3 shows temperature calibration curves up to 2000 °C as a function of applied load, which was determined in a separate no-X-ray experiment with W5%Re–

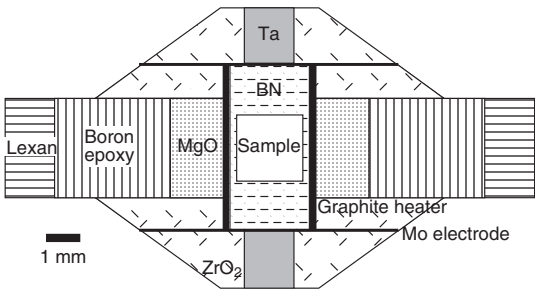


**Fig. 2.** A schematic illustration of a standard cell assembly for liquid structure and/or viscosity measurements.

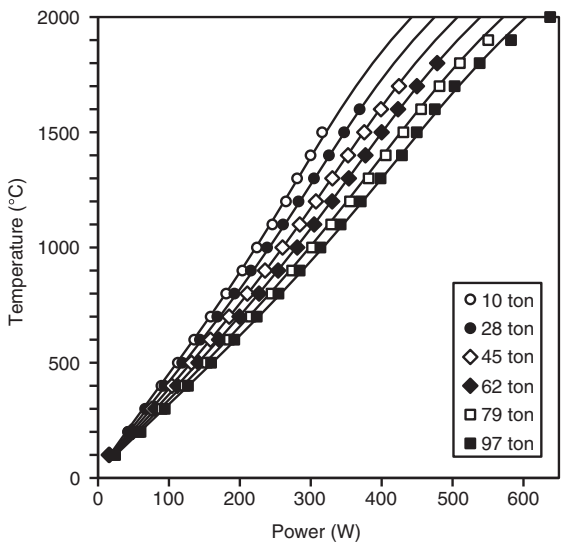


**Fig. 3.** Temperature-power relation measured up to 2000 °C and 97 ton hydraulic load (~7 GPa in sample pressure). The curves represent the results of fitting for the experimental results to two dimensional (power and load) polynomial equation.

Author's personal copy



W26%Re thermocouple. The thermocouple was inserted at the center of the standard cell assembly. We fit these data to a two dimensional (power and load) polynomial equation and used these temperature calibration curves to estimate temperature in liquid structure measurement.

The MgO ring is also used as the pressure standard by using an equation of state (Kono et al., 2010). Uncertainty of the pressure calculation using the MgO ring was typically up to 0.15 GPa. However, since the closest MgO position is 1.4 mm from the center of the sample, pressure and/or temperature gradients may exist between the MgO ring and the sample. We have measured the pressure difference between the MgO ring position and the center of the cell assembly (Fig. 4), by using MgO powder as the sample at the center of the cell assembly to investigate the pressure difference, with temperature measured by a W5%Re–W26%Re thermocouple placed just below the MgO sample. At room temperature, we found no marked pressure difference between the MgO ring and the center of the cell assembly under compression. During the first heating up to ~1000 °C, there was also no pressure difference. Above 1000 °C, however, pressure at the sample center position ($P_{sample}$) became lower than that of MgO ring ($P_{ring}$). After heating, $P_{sample}$ and $P_{ring}$ are different even at room temperature. We observed a linear relation between $P_{sample}$ and $P_{ring}$ after the first heating above 1000 °C and during subsequent heating. There was no obvious change in the linear relationship with pressure between 0.8 and 5 GPa. The linear relationship between $P_{sample}$ and $P_{ring}$ above 1000 °C can be well expressed by $P_{sample} - P_{ring} = 7.7–8.3 \times 10^{-4} \times T$, where T is temperature in °C. On the other hand, pressure gradient inside the sample is insignificant (Fig. 5). Pressure difference inside a 1.6 mm diameter sample up to 5 GPa and 800 °C by using equation of state of NaCl (Matsui, 2009) is within 0.3 GPa.

Fig. 6a shows room temperature high-pressure generation in the standard cell assembly together with some recent test results using smaller size anvils. The standard cell assembly using 12 mm cup anvils (Fig. 6b) is capable of generating pressures to around 7 GPa at room temperature. The use of smaller anvil sizes increases pressure efficiency. For instance, the use of 8 mm cup anvils (Fig. 6c) results in a ~40% increase in pressure efficiency (Fig. 6a). In order to further increase pressure efficiency, we have

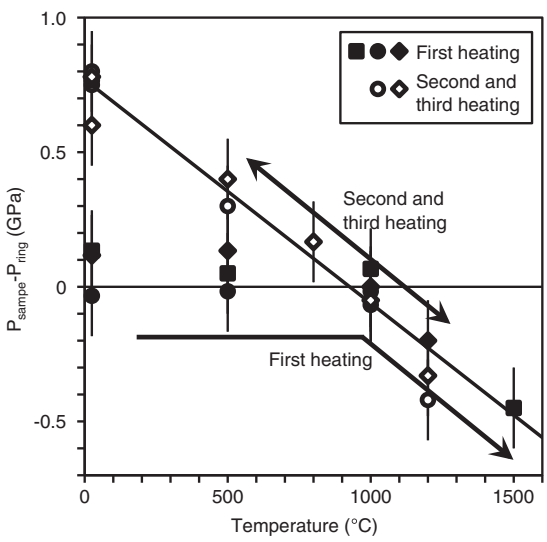


**Fig. 4.** Pressure difference between sample and MgO ring (1.4 mm apart from the sample center) positions ($P_{sample} - P_{ring}$). There was no observable pressure difference at the first heating below 1000 °C. In contrast, a linear relation in the $P_{sample} - P_{ring}$ was found at temperatures above 1000 °C in the first heating and subsequent heating cycles.

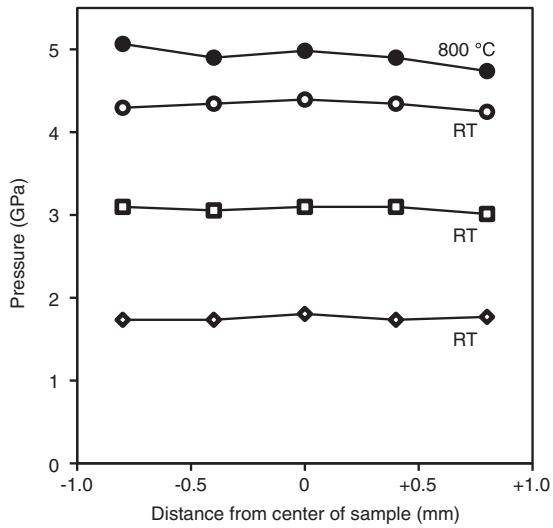


**Fig. 5.** Pressure gradient inside sample (1.6 mm diameter). No observable pressure gradient was found up to ~5 GPa and 800 °C.

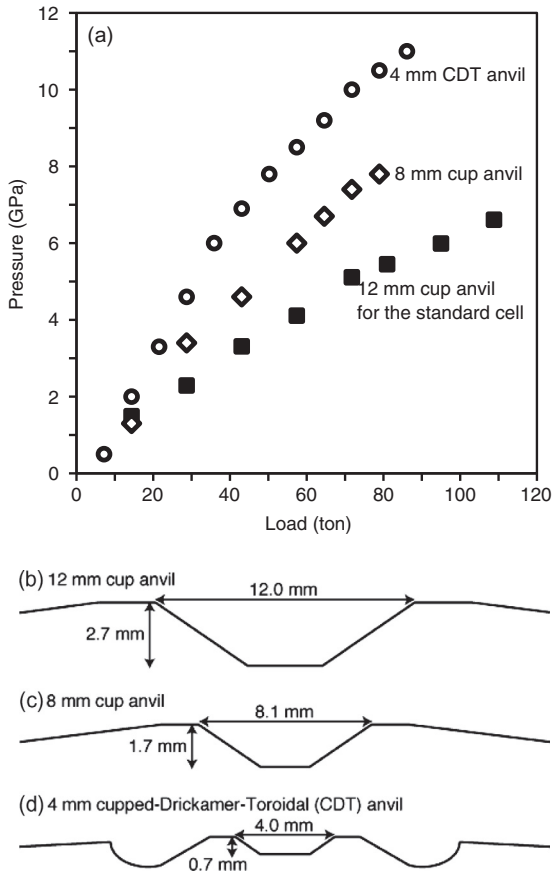


**Fig. 6.** Pressure generation curves of the standard cell assembly (12 mm cup anvil), and smaller size anvils (8 mm cup anvil and 4 mm CDT anvil) (a) with the design of the 12 mm cup (b), 8 mm cup (c), and 4 mm CDT anvils (d).

tested a newly designed anvil geometry. A recent study of Gotou et al. (2011) succeeded in generating 15 GPa and 1427 °C with >1 $mm^3$ sample volume by using cupped Drickamer-type anvils. However, the Drickamer-type apparatus requires a confinement ring, which severely restricts the available range of $2\theta$ angle. On the other hand, Shchennikov et al. (2008) suggested a composite high-pressure cell, which is a modification of a Drickamer-type cell

Author's personal copy



without the external supporting ring. They apply a Toroid-like gasket setup, which provides 360° horizontal opening, similar to the Paris–Edinburgh cell. We combine these two ideas to generate high pressures and high temperatures with wide horizontal opening for multi-angle EDXD measurement (Fig. 6d). The new anvils have enabled us to generate high pressures more than 10 GPa (Fig. 6a). On the other hands, use of sintered diamond anvil instead of WC anvil would further increase pressure generation capability as Morard et al. (2007) generated up to 16.5 GPa using 5 mm cup diameter sintered diamond anvil.

## 4. Structural measurements for liquids

The multi-angle energy dispersive X-ray diffraction (EDXD) technique is employed for measuring liquid structures. Principles of the method are thoroughly explained in many references (Egami, 1978; Waseda, 1980; Nishikawa and Iijima, 1984; Hosokawa et al., 1991; Sugiyama et al., 1996). Here, we only brief the application at 16BM-B beamline.

### 4.1. Diffractometer setup and collimation depth control

Fig. 7 illustrates the default optical components of EDXD setup in 16BM-B experimental hutch. The incident white X-ray is unfocused, linearly polarized. The first slits are located approximately 25 m from the source, defining the incident beam position and size onto the sample. The second silts are adjacent to the first slits, the gaps of which are adjusted to be 10% larger, to clean up scatter from the primary slits. The typical beam size is 0.1 mm (h) × 0.3–0.5 mm (v). A tungsten beam stop blocks the pass-through beam after the sample, to eliminate secondary background scatter (e.g., tungsten fluorescence from the slits in front of the detector).

For diffracted X-rays, two slits are located on the diffractometer arm: one near the sample (around 60 mm from the center) and the other in front of the detector (at around 480 mm distance). The detector arm also supports the Ge-SSD with a liquid nitrogen dewar. To minimize any dynamic eccentricity while changing $2\theta$, the $2\theta$ diffractometer rotates in the horizontal plane on air pads supported by a granite table (Fig. 1).

Because the collimation depth is projected through the width of incident beam, the total collimation depth increases substantially when increasing the incident beam width, especially, at low angles. This effect is illustrated in Fig. 7 by comparison of $D_0$ (without considering the beam width) and $D_1$ (when considering the beam width). The divergence of collimated beam is negligible in practice due to the large aspect ratio between slit gaps (typically <0.1 mm) and the slit distances (400–420 mm from each other), i.e., <0.03°. Fig. 8 shows calculated collimation depth with 0.05 and 0.1 mm collimator slit gaps at 60 mm distance from the diffractometer center and a 0.1 mm second diffraction slit gap at 480 mm distance as a function of $2\theta$ angles. The effect of incident beam size on the total collimation depth ($D_1$) is illustrated for 0.1 mm beam sizes. For the 0.1 mm incident beam size and 0.05 mm collimator slit gap, around 63–71% of volume is in $D_0$. The effective collimation depth can be controlled by adjusting the incident beam size, slit gaps and distances from the diffractometer center.

The collimation depth control is important to liquid scattering measurement for discriminating sample signal from background scattering caused by surrounding materials. For example (Fig. 8), with 0.05 mm collimator, 0.1 mm detector slit, and 0.1 mm incident beam size, the collimation depth at $2\theta = 10°$ is around 1 mm (grey solid line). If the sample diameter is 1 mm or larger, the measured scattering intensities at and above this angle originate only from the sample. The tight control of collimation depth is essential to obtain reliable structure data for liquids as the signals are diffused and weak. For monochromatic beam diffraction with a large area detector, a multichannel Soller slit has been developed to implement the collimation depth control (Mezouar et al., 2002; Morard et al., 2011).

### 4.2. Scattering data analysis

The observed energy dispersive X-ray diffraction spectrum at a given $2\theta$ angle can be described:

$$I_m(2\theta, E) = s(2\theta)P(2\theta)A(2\theta, E)C(E)I_p(E)[I_{\mathrm{coh}}(2\theta, E) + I_{\mathrm{inc}}(2\theta, E)] \quad (1)$$

where, $s(2\theta)$ is a scale factor, $P(2\theta) \approx \cos^2(2\theta)$ the polarization factor for linearly polarized synchrotron beam in horizontal plane, $A(2\theta,E)$ the X-ray attenuation, $C(E)$ any other energy dependent term (e.g., detector efficiency), $I_P(E)$ the primary white beam profile, $I_{\mathrm{coh}}(2\theta,E)$ and $I_{\mathrm{inc}}(2\theta,E)$ are the coherent and incoherent scattering from the sample, respectively. Practically, the polarization factor is a constant at a fixed $2\theta$ angle and the angle dependence of X-ray attenuation disappears for a cylindrical sample (i.e., $A(2\theta,E) \rightarrow A(E)$). Thus, the Eq. (1) can be effectively rewritten as

$$I_m(2\theta, E) = s'(2\theta)I_{P,\mathrm{eff}}(E)[I_{\mathrm{coh}}(2\theta, E) + I_{\mathrm{inc}}(2\theta, E)] \quad (2)$$

where, $s'(2\theta) = s(2\theta)\ P(2\theta)$ and $I_{P,\mathrm{eff}}(E) = A(E)C(E)\ I_P(E)$, respectively. Fig. 9a shows an example of measured EDXD spectra from $SiO_2$ glass at multiple discrete $2\theta$ angles. For these spectra, the effective primary beam, $I_{P,\mathrm{eff}}(E)$, cannot be separately measured, therefore an approximation is made using the measured spectrum at the highest

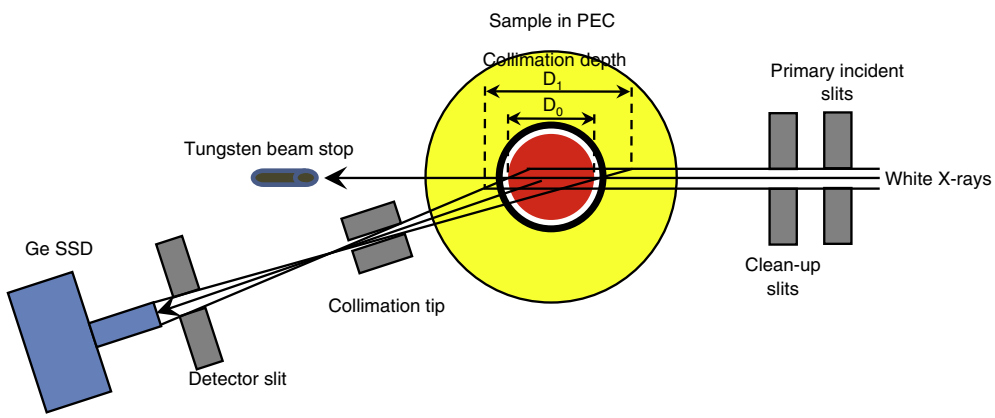


**Fig. 7.** A schematic of drawing of HPCAT 16BM-B white X-ray energy dispersive X-ray diffraction setup and the concept of collimation depth defined by slit geometry. ($D_o$: collimation depth at the beam center; $D_1$: collimation depth elongated due to the practical beam width).

Author's personal copy



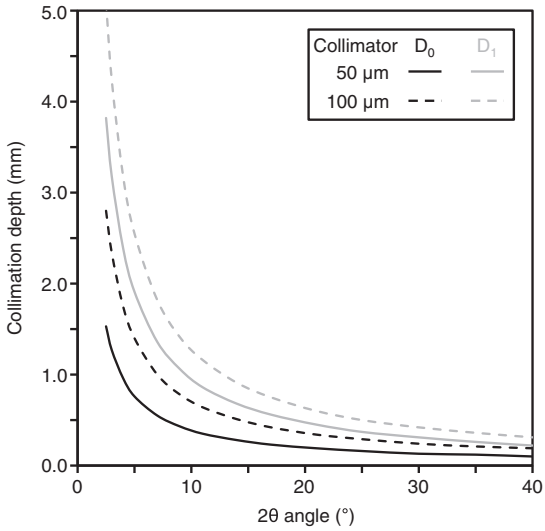


**Fig. 8.** Comparison of collimation depth variation as a function of $2\theta$ angles between two different collimator slit widths (50 μm and 100 μm) with 100 μm incident beam width. Note the significant difference between $D_o$ and $D_1$ variations as defined in Fig. 7.

$2\theta$ angle (34.9°) by a non-linear least square fitting with a polynomial function. For the best approximation, only a limited range of energy is chosen and the unknown $I_{coh}(2\theta,E)$ is replaced with calculated $<f^2(2\theta,E)>$ to ignore the persisting oscillatory features observed even at this high diffraction angle, which is supposed to be the intrinsic structure of the $SiO_2$ glass. Here,

$$\langle f^2(2\theta, E)\rangle = \langle f^2(q)\rangle \equiv \sum_i c_i f_i^2(q), \tag{3}$$

$$I_{inc}(2\theta, E) = I_{inc}(q) \equiv \sum_i c_i I_{i,Compton}(q), \tag{4}$$

$$q = \frac{4\pi \cdot E}{12.3984}\sin(\theta), \tag{5}$$

where, $c_i$ is the atomic fraction and $f_i(q)$ the atomic scattering factor of $i$-th element, respectively. The parameters to calculate $f(q)$ and $I_{Compton}(q)$ are from International Tables for X-ray Crystallography (Ed. Ibers and Hamilton) and Refs. (Cromer and Mann, 1967; Cromer, 1969), respectively. Fig. 9b illustrates the approximation of the measured EDXD spectrum at the highest $2\theta$ angle (34.9°) using the polynomial function and Eqs. (3), (4). Note that the low limit of the effective primary beam estimation is chosen to avoid the distinct oscillatory features below it. On the other hand, the high limit is chosen to reject instrument-induced systematic errors (in our case, the step around $E = 69$ keV is due to the tungsten absorption edge caused by the slits). The ideal energy range and the polynomial order are typically determined through "try-and-error" approaches in practice. The $I_{P,eff}(E)$ is typically modeled with 3-rd to 5-th order polynomial function.

The Faber-Ziman type structure factor for liquid is defined as:

$$S(q) = \frac{I_{coh}(q) - \langle f^2(q)\rangle}{\langle f(q)\rangle^2} + 1 \tag{6}$$

where, $\langle f(q)\rangle \equiv \sum_i c_i f_i(q)$. For each measured spectrum at different $2\theta$ angles, a fragmented structure factor $S(q) = S(2\theta,E)$ can be estimated using the estimated $I_{P,eff}(E)$ as follows:

$$S(q) = S(2\theta, E) = \frac{I_m(2\theta, E) - s'(2\theta)I_{P,eff}(E)\left[\langle f^2(2\theta, E)\rangle + I_{inc}(2\theta, E)\right]}{s'(2\theta)I_{P,eff}(E)\langle f(2\theta, E)\rangle^2} + 1 \tag{7}$$

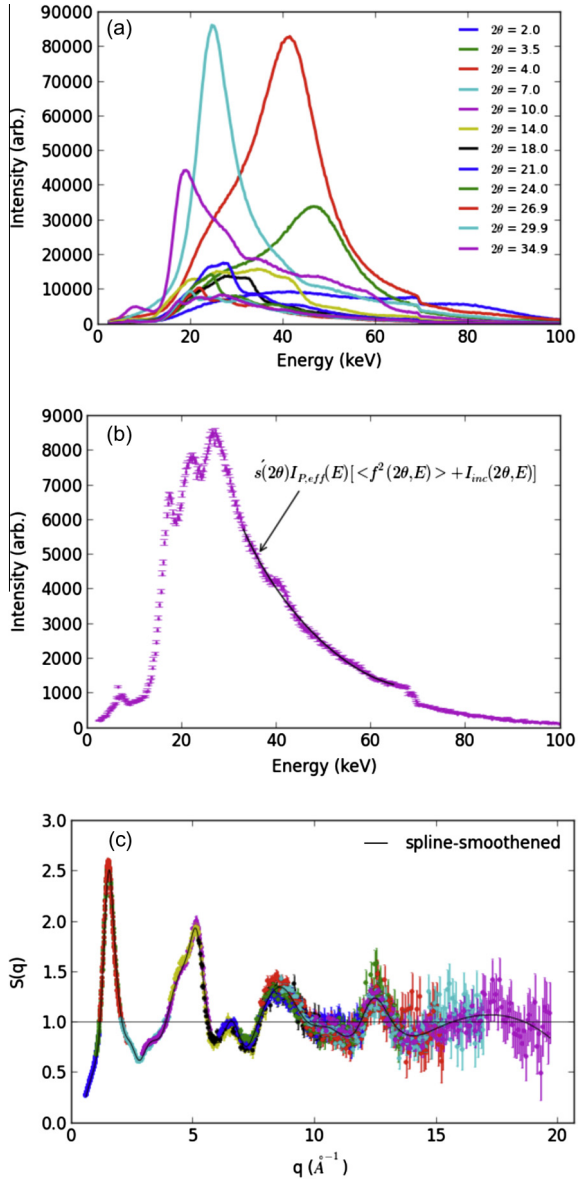


**Fig. 9.** (a) Energy dispersive X-ray diffraction spectra measured from $SiO_2$ glass mounted in air at $2\theta = 2.0°$ (200 s), 3.5° (200 s), 4.0° (400 s), 7.0° (400 s), 10.0° (600 s), 14.0° (600 s), 18.0° (600 s), 21.0° (900 s), 24.0° (900 s), 26.9° (900 s), 29.9° (1200 s), and 34.9° (1200 s), where the number in parenthesis is the exposure time; (b) the effective primary beam estimation using the highest $2\theta$ angle spectrum for a selected energy range; (c) total structure factor S(q) composed of the fragmented structure factor scaled with respect to the highest angle fragment. The solid line is obtained for evenly spaced q values after error-weighted spline-smoothening of the overlapped structure factor fragments.

These fragmented structure factors are to be rescaled in reverse sequential order with respect to the one obtained at the highest $2\theta$, which oscillates around one by definition from the above described procedure to determine $I_{P,eff}(E)$, and merged in a consistent $S(q)$. Fig. 9c demonstrates how each fragmented structure factors, $S(2\theta,E)$, are scaled and merged. The necessary number of $2\theta$ angles (i.e., the number of fragmented structure factors) to complete the structure factor is an arbitrary choice depending on the system to be measured and the instrumental setup (especially, the available energy range of the primary beam estimation in this particular approach). A typical set includes eight to twelve spectra at HPCAT 16BM-B beamline. An evenly spaced $S(q)$ in $q$-space can be obtained from the merged structure factor data after error-weighted spline-smoothening.

Author's personal copy



The error-bars in Fig. 9c are rigorously propagated from the counting statistics of the raw data, assuming the counting probability follows the Poisson distribution, and convoluted with the uncertainty involved in the primary beam estimation and the scaling procedures. The increasing errors with increasing $q$ arise from the effect of atomic scattering factor for X-rays decaying with $q$ and being further weighted with the shape of primary beam profile. The required counting statistics to compensate this effect should be proportional to $1/\langle f^2(q)\rangle$, which is impractical, therefore the practical limit of the $S(q_{max})$ is often chosen smaller than the instrumental limit (e.g., $q_{max} = \sim 19$ Å$^{-1}$ at $2\theta_{max} = 34.9°$ and $E_{max} = 65$ keV for the primary beam estimation in this example). The maximum $q_{max}$ defines the resolution width in real space, $\Delta r = \pi/q_{max}$, thus the limited $q_{max}$ also limits the finest features that can be observed in the real space distribution of pair distribution function.

From an evenly spaced $S(q)$, a pair distribution function $G(r)$ is obtained as:

$$G(r) = \frac{2}{\pi}\int_{q_{min}}^{q_{max}} q[S(q) - 1]\sin(qr)\mathrm{d}q \tag{8}$$

Note that, if the oscillatory features of structure factor persist at the $q_{max}$, the result of Eq. (8) will generate "ghost ripples" in the pair distribution function, of which the period corresponds to $2\pi/(q_{max} - q_{min})$ and may interfere the oscillations representing the true atomic correlations. A well accepted practice to characterize these non-intrinsic oscillations is to multiply a resolution broadening correction function, known as the Lorch function, $\left[\frac{\sin(q\Delta r)}{q\Delta r}\right]$ to the structure factor before the integration. This modification function effectively removes the ghost ripples in the pair distribution function so that can be very useful to discriminate out the true atomic correlations from an artifact. However, the convenience is obtained at the cost of an enforced damping of the signals; therefore its application must be carefully made not to diminish the true signals in the pair distribution function.

### 4.3. In-situ measurement in PE cell

In order to verify the efficacy of the above mentioned collimation depth control and data reduction procedure, the experimental $S(q)$ and $G(r)$ of $SiO_2$ glass in air and in PE cell at ambient pressure are directly compared in Fig. 10a and b. The data from $SiO_2$ glass in air represents reference $S(q)$ and $G(r)$ obtained without the influence of X-ray attenuation by the PE cell sample assembly materials, which is the only but significant variation in Eqs. (1) and (2) modifying the measured spectral shape. In the $S(q)$, there is a small deviation between two data sets; however the corresponding $G(r)$ functions reveal that the deviation is largely due to the artifacts which generates unphysical density oscillation below the hard-core limit of atomic correlation distances. The errors below the hard-core limit can be corrected by Kaplow-type iterative error correction procedures (Kaplow et al., 1965; Eggert et al., 2002). Regardless, the true comparison is made in the $G(r)$, which shows almost identical oscillations in the pair distribution functions within the errors without the Kaplow iterative error correction. Note that the errors indicated in $G(r)$ function are also propagated though the Fourier transformation of $S(q)$, and substantially reduced over the entire range of displayed $r$. The reduced error is attributed to the effect of Lorch modification function (the comparison between with and without the Lorch function modification on the size of error in $G(r)$ has been made separately, not shown here).

With the known average number density of $SiO_2$ glass at room temperature and atmospheric pressure ($\rho_o = 0.0796$/Å$^3$), the radial distribution function, $4\pi r^2\rho_o\ G(r) \equiv 4\pi r^2\rho_o + rG(r)$, can be calculated (Fig. 10c), under this curve the integrated area corresponds to the average pair coordination numbers. For the first peak (corresponding to Si–O distance), a Gaussian fitting generates the peak positions, coordination numbers, and root mean square distribution widths to be 1.635 ± 0.006 Å, 3.96 ± 0.14, and 0.139 ± 0.006 Å, respectively, for the in-air $SiO_2$ glass, and 1.633 ± 0.007 Å, 3.74 ± 0.16, and 0.139 ± 0.007 Å, respectively, for in-PE cell $SiO_2$ glass, respectively. All the structural parameters are identical within the estimated errors; therefore the experimental determination of amorphous structure in PE cell *in situ* is well verified.

## 5. Ultrasonic elastic wave velocity measurement

A 10°Y-cut $LiNbO_3$ transducer, which generates and receives both compressional and shear waves simultaneously, is attached to the back side of the top WC anvil and connected to a co-axial cable, which goes through a hole at the top of the PE press (cf. Kono et al., 2012). 20 MHz (for shear wave) and 30 MHz (for compressional wave) electrical sine waves generated by a pulse generator (Tektronix AFG3251) are divided into two directions by a directional bridge (Agilent RF Bridge 86205A). One signal is directed to the oscilloscope through a −40 dB attenuation path and the other signal goes to the $LiNbO_3$ transducer through the directional bridge.

In order to transmit elastic waves to the sample, an $Al_2O_3$ buffer rod is placed between the WC anvil (with the acoustic transducer) and the sample (Fig. 11). Elastic waves pass through the WC anvil, propagate through the $Al_2O_3$ buffer rod and enter the sample. A series of reflected elastic wave signals come from the interfaces of anvil/buffer rod (R0), buffer rod/sample (R1), sample/$Al_2O_3$ plate (R2), and $Al_2O_3$ plate/BN pressure medium (R3) (Fig. 11). These series of reflected signals and the attenuated input signal are amplified by a 40 dB amplifier with a bandwidth of 0.2–40 MHz (Olympus Model 5678 Ultrasonic Preamplifier) and acquired with a sampling rate of $10 \times 10^9$ sample/s (0.1 ns interval at each sampling) by a digital oscilloscope (Tektronix DPO5104). The elastic wave travel time is determined by the pulse echo overlap method using the reflected signals from the buffer rod/sample (R1) and sample/backing reflector (R2) interfaces (Figs. 11 and 12). Then, elastic wave velocity is calculated using the elastic wave travel time and sample length determined by X-ray radiography measurement. Details of the elastic wave velocity measurement and analytical method were described in Kono et al. (2012).

We have succeeded in conducting ultrasonic measurements not only on solid materials but also liquids. Fig. 12 shows an example of compressional and shear wave form change across the melting of germanium. Signals obtained for solid germanium at 700 °C show clear R1 and R2 reflections for both compressional and shear waves. In contrast, R2 shear wave signal disappears after melting of germanium at 780 °C. In addition to the disappearance of R2 shear wave signal, a significant increase in amplitude of R1 shear wave signal can be seen. This is attributed to complete reflection of shear wave energy at the top of liquid germanium. Similar to the R1 shear wave signal, a marked increase in amplitude of R1 compressional is observed, because of significant change in the acoustic impedance (=density × compressional wave velocity) of germanium by melting and the resultant change of the reflection coefficient between alumina rod and germanium sample (=$(Z_a - Z_g)/Z_aZ_g$, where $Z_a$ and $Z_g$ are acoustic impedance of alumina rod and germanium sample, respectively). In addition, a significant increase in travel time delay between R1 and R2 reflections is observed for compressional wave. Fig. 13 shows compressional wave velocity change of solid and liquid germanium with varying temperature at ~4.5 GPa. Compressional wave velocity in solid germanium decreases slightly with increasing temperature. Then,

Author's personal copy



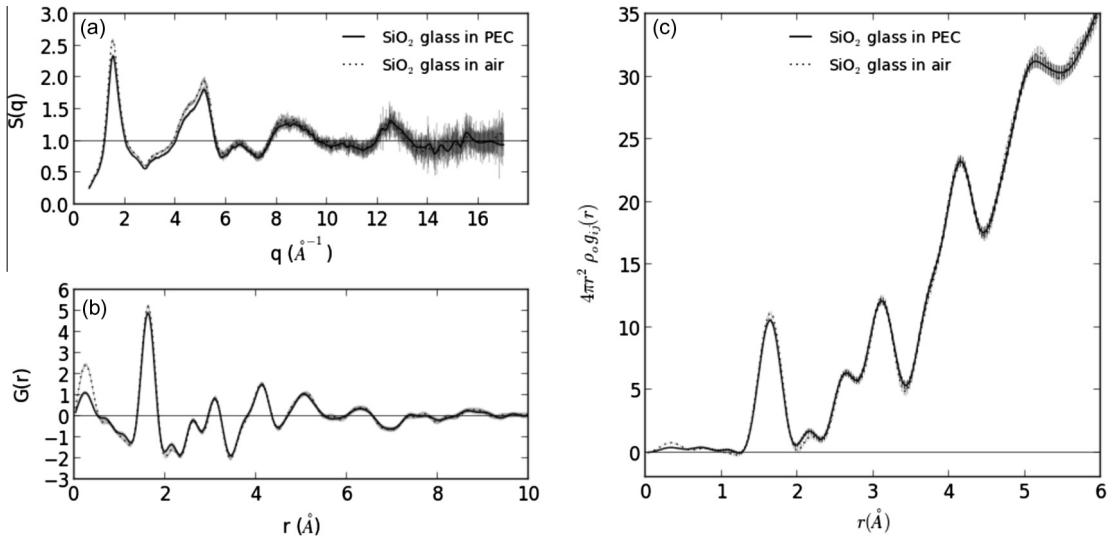


**Fig. 10.** Comparison of (a) structure factor S(q), (b) reduced pair distribution function $G(r)$ with applying the Lorch modification function, and (c) the radial distribution function obtained using the known density, between $SiO_2$ glass measured in air and in PEC at room pressure and temperature. The results are identical within statistical errors, verifying the efficacy of the data reduction process described in Section 4.2 for *in situ* PEC experiment for determining amorphous/liquid structures in general.

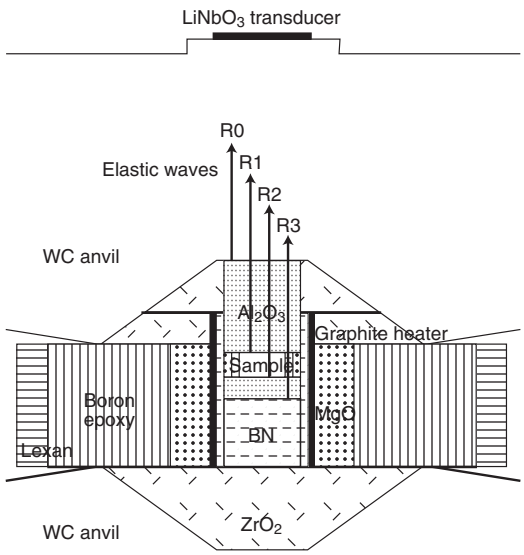


**Fig. 11.** High-pressure cell assembly and WC anvil for ultrasonic measurement. $LiNbO_3$ transducer attached behind the WC anvil generates and receives elastic waves.

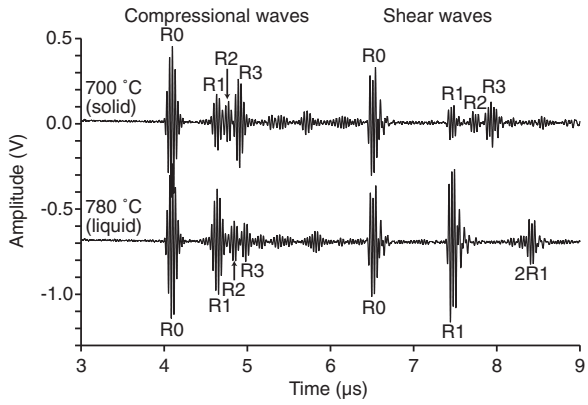


**Fig. 12.** Examples of longitudinal and transverse wave signals obtained for solid and liquid germanium at 700 and 780 °C, respectively. The R0, R1, R2, and R3 signals represent reflected elastic waves at anvil/buffer rod (R0), buffer rod/sample (R1), sample/$Al_2O_3$ plate (R2), and $Al_2O_3$ plate/BN pressure medium (R3) interfaces, respectively.

compressional wave velocity significantly decrease from 5.84 km/s at 700 °C to 3.50 km/s at 780 °C due to melting of germanium.

## 6. White X-ray radiography

White X-ray radiography is used to image the interior of the cell assembly at high pressures, and is mainly used for travel distance determination for elastic wave velocity measurements (Section 5) or falling sphere viscosity measurement (Section 7). Details of high-speed camera setup are described in the Section 7. Here we describe static, high-resolution X-ray radiography measurement using a high depth-resolution (12 bit) CCD camera.

Wide white beam up to 1.8 mm in both vertical and horizontal directions is available for X-ray radiography measurement in the 16-BM-B station. We use Eu-doped lutetium aluminum garnet (LAG:Eu) as a scintillator, which is located at around 30 cm distance from the sample, with a 45° mirror and a 10 times infinity-corrected objective lens (numerical aperture = 0.28) mounted on a 127 mm long tube. The CCD camera (Prosilica GC1380) has 1360 (horizontal) × 1024 (vertical) pixels. The pixel resolution is calibrated by using a WC ball with 497 μm diameter, yielding 0.95 μm/pixel, corresponding to approximately 1.3 (horizontal) × 1.0 (vertical) mm full field of view. Typical exposure time of the white X-ray radiography measurement is around 0.5 s.

Fig. 14 shows an X-ray radiography image of a WC plate edge (Fig. 14a), an edge profile (Fig. 14b), and the resultant line spread function (Fig. 14c) obtained by taking the derivative of the edge profile. The line spread function shows a sharpness of ~4 pixel (=~4 μm) for the intrinsic imaging resolution of our white X-ray radiography system, defined at the full width of the half maximum (FWHM). Fig. 14d and e show a more practical example of WC sphere placed in a hole in a grassy carbon rod. The line profile also shows sharp brightness change in ~4–5 pixel at the edge of WC ball. The sensitivity for relative motion of moving objects is calibrated by using a high-precision linear stage with 1 μm step size for the WC plate (Fig. 15). Regardless of the image resolution, the

Author's personal copy



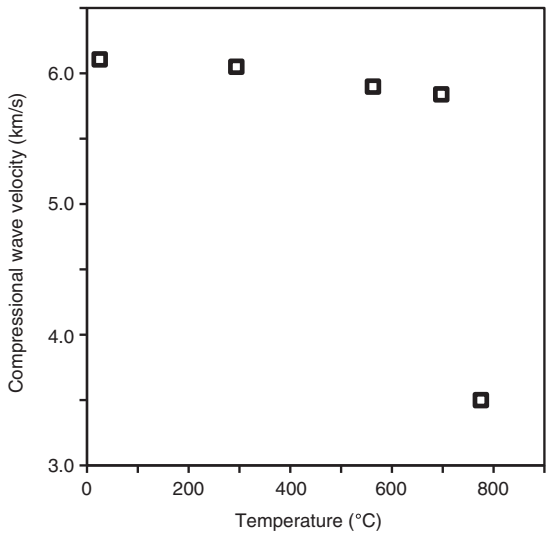


**Fig. 13.** Compressional wave velocity of germanium as a function of temperature. Melting of germanium at ~780 °C causes strong decrease in compressional wave velocity.

15 repeated tests show that our X-ray radiography setup can detect 1 μm motion with 1$\sigma$ standard deviation of 0.1 μm.

## 7. Liquid viscosity measurement

High-pressure liquid viscosity is measured using the falling sphere viscometry technique either by quench experiment (e.g., Kushiro et al., 1976; Sharma et al., 1979) or combined with *in situ* synchrotron X-ray radiography measurement (e.g., Kanzaki et al., 1987; Dobson et al., 2000; Terasaki et al., 2001, 2006). The viscosity ($\eta$) can be calculated with the Stokes' equation by using the terminal velocity of falling sphere ($v$) with correction factors for wall effect ($F$) (Faxén, 1922) and end effect ($E$) (Maude, 1961):

$$\eta = \frac{g d_s^2 (\rho_s - \rho_l)}{18 v} \frac{F}{E} \tag{9}$$

$$F = 1 - 2.104\left(\frac{d_s}{d_l}\right) + 2.09\left(\frac{d_s}{d_l}\right)^3 - 0.95\left(\frac{d_s}{d_l}\right)^5 \tag{10}$$

$$E = 1 + \frac{9}{8}\frac{d_s}{2Z} + \left(\frac{9}{8}\frac{d_s}{2Z}\right)^2 \tag{11}$$

where $\rho$ and d are density and diameter, with subscripts s and l denoting properties of probing spheres and liquid, respectively. $Z$ is the sample height.

In order to determine viscosity reliably using Eq. (9), precise measurements of the diameter of the probing sphere ($d_s$), density difference between the probing sphere and the liquid sample ($\rho_s - \rho_l$), and the falling sphere terminal velocity ($v$) are important. The precision of the sphere diameter depends on the resolution of the X-ray radiography measurement. Here we use the high-resolution camera placed at the position closet to the sample (cf. Section 6) in order to precisely determine the diameter of the sphere. Although the density of the sphere can be precisely calculated using the equation of state of the probing sphere material (e.g., platinum, rhenium, and so on), it is difficult to measure liquid density *in situ* combined with the viscosity measurement, because of technical difficulties (e.g., Katayama et al., 1998; Shen et al., 2002; Ohtani et al., 2005). Fortunately, uncertainty of liquid density can be minimized by adopting a sphere material having a significantly different density than the liquid density. For example, in

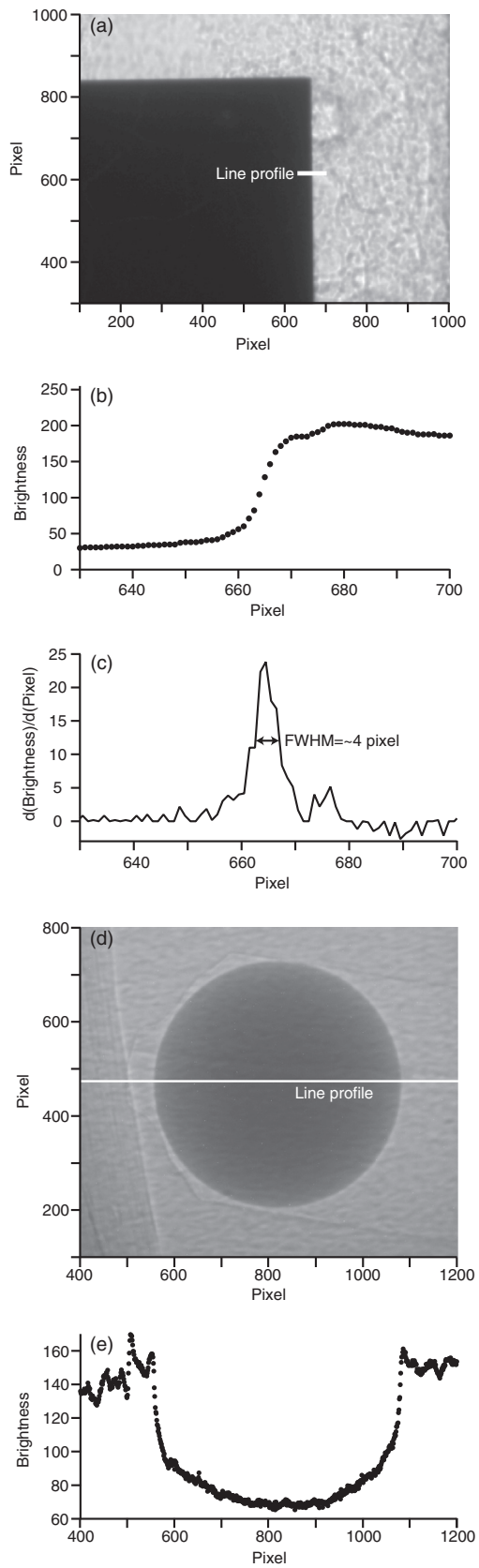


**Fig. 14.** X-ray radiography image of WC plate edge (a), an edge line profile (b), and the resultant line spread function observed by derivative of the edge profile (c). (d) and (e) represent X-ray radiography image and line profile through 497 μm WC ball, respectively. Dark area at the left side of Fig. 14d is attributed to a tape used to fix WC ball on stage. The WC ball was placed in a hole (horizontal direction) drilled in grassy carbon rod.

Author's personal copy



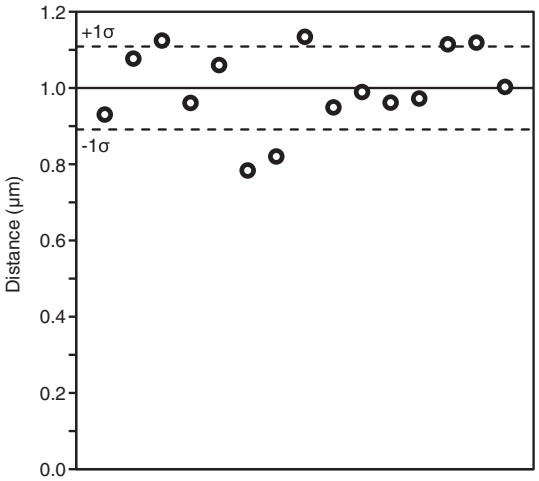


**Fig. 15.** Distance of 1 μm step motion measured by the X-ray radiography. Dashed lines represent ±1σ standard deviation of 0.1 μm.

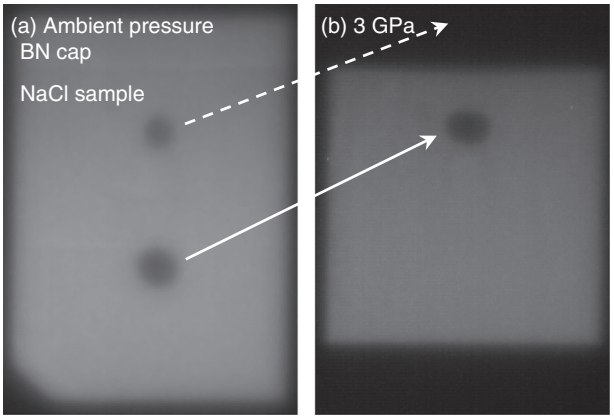


**Fig. 16.** X-ray radiography images of two Pt spheres in NaCl sample at ambient pressure (a) and at 3 GPa (b) in a viscosity measurement. The Pt sphere placed around the top of the sample was hidden by the top WC anvil at 3 GPa.

the case of a Pt sphere (21.45 g/cm$^3$ at ambient condition) in liquid NaCl sample (1.547 g/cm$^3$ at ambient condition) (Kono et al., 2013), a 10% difference in liquid density will influence the viscosity by 0.8%.

It has been pointed out that uncertainties in terminal velocity play a dominant role in the precision of the viscosity determination (Brizard et al., 2005). The precision of terminal velocity measurement depends primarily on the camera frame rate. Previous high-pressure viscosity measurements were conducted using limited imaging rates (typically from ~30–60 to 125 frames/s, or fps), which are suitable only for highly viscous materials such as silicate or oxide melts. Some studies report viscosities in the 4–20 mPa s range for iron alloy melts (Dobson et al., 2000; Terasaki et al., 2001) using falling sphere velocities determined based on only 2–4 images. This limited imaging rate makes it difficult to ensure that the falling sphere has reached terminal velocity and results in large uncertainties in the calculated viscosity. The high-speed camera (Photron FASTCAM SA3) that we have installed can collect images at a rate of more than 1000 fps and is ideal for precise viscosity measurements on low viscosity materials at high pressures (Kono et al., 2013). The high-speed camera has a maximum image size of 1024 pixels in both horizontal and vertical and is located ~1.2 m downstream from the PE cell. Variable pixel sizes of 2.8–5.9 μm/pixel are available by using 5 or 10 times infinity-corrected objective lenses combined with lens tube lengths of 25–90 mm.

We generally use two Pt spheres in each falling sphere viscosity measurement (Fig. 16): one is located near the center of the sample to identify melting of the sample and to trigger the high-speed camera (sphere 1), the other is placed at the top of the sample to measure velocity of the probing sphere over the longest travel distance possible (sphere 2). This two-ball approach is necessary because the sphere at the top of the sample is hidden by the top WC anvil at high pressures (Fig. 16b). In addition, falling of the Pt sphere over the longest distance is important to achieve terminal velocity.

Fig. 17 shows a series of images of falling of Pt spheres in liquid NaCl recorded at 2000 fps with an exposure time of 0.5 ms per frame. Sphere 1 at the center of the sample fell immediately after melting of the NaCl sample. However, the trajectory of this sphere was not linear. It first fell almost straight at around 8–16 ms, and then started to move toward left (Fig. 17a). The velocity of falling sphere first increased with distance before around 15 ms to reach a more or less constant value, but then to decreased after around 15 ms (Fig. 17b). Finally, velocity of falling sphere became constant. In contrast, sphere 2 shows excellent linearity in the sphere travel distance with time, indicating that terminal velocity has been achieved (Fig. 17c and d). Note that the terminal velocity obtained by the falling of sphere 2 is markedly different from the final velocity obtained from the falling of sphere 1 (Fig. 17b and d). Although different size of sphere 1 and 2 should cause difference in the falling velocity, sphere 1 should have even higher falling velocity than that of sphere 2 because of larger sphere diameter.

We consider the leftward motion of sphere 1 to be the cause of slower terminal velocity of sphere 1. This leftward motion may be due to remnant of solid NaCl near the bottom (and top) center of the sample (Fig. 18). Because sphere 1 was located around the center of the sample, where the highest temperature is expected, and likely melting of NaCl was first reached, and sphere 1 started falling immediately after melting. In contrast, the time duration of several milliseconds may not be enough to equilibrate temperature in the entire sample, and therefore temperature at the bottom (and top) of the sample may be still lower than the melting temperature of NaCl. The remnant of solid NaCl interfered straight falling of the sphere 1, and sphere 1 might fell along the slope of the solid NaCl (Fig. 18a). Thus, the final velocity observed in the falling of sphere 1 may be velocity of rolling sphere on solid NaCl slope, and therefore the velocity was significantly slower than the terminal velocity obtained by the falling of sphere 2.

In contrast, sphere 2 started falling several seconds after the start of falling of sphere 1 (=start of melting at the center of the sample). When sphere 1 started falling, sphere 2 would locate in solid NaCl at the top of the sample (Fig. 18a). Then, heat diffuses to the top and bottom of the sample with time, and sphere 2 starts falling when the top part of the solid NaCl sample melts. Similarly, the bottom solid NaCl should have been molten when the top NaCl is molten (Fig. 18b). Therefore, sphere 2 fell smoothly in almost completely molten NaCl sample, and falling of the sphere 2 showed excellent linearity in the sphere travel distance with time. Because this process happened at a constant heater power condition with time, we consider that the delay of melting at the top and bottom of the sample would be attributed to time delay of heat transfer.

Thus, it is important to monitor the motion of falling sphere with substantial oversampling in order to determine terminal velocity accurately. The high-speed camera that can collect images at more than 1000 fps plays important role to monitor the motion of falling sphere. Problem of incomplete melting of sample may be solved by overheating of sample above melting temperature. For example, some studies placed high melting temperature material above sample with probing sphere, and release the probing sphere by melting of the high melting temperature material (e.g., Terasaki et al., 2001; Liebske et al., 2005). By using this method, it is possible

Author's personal copy



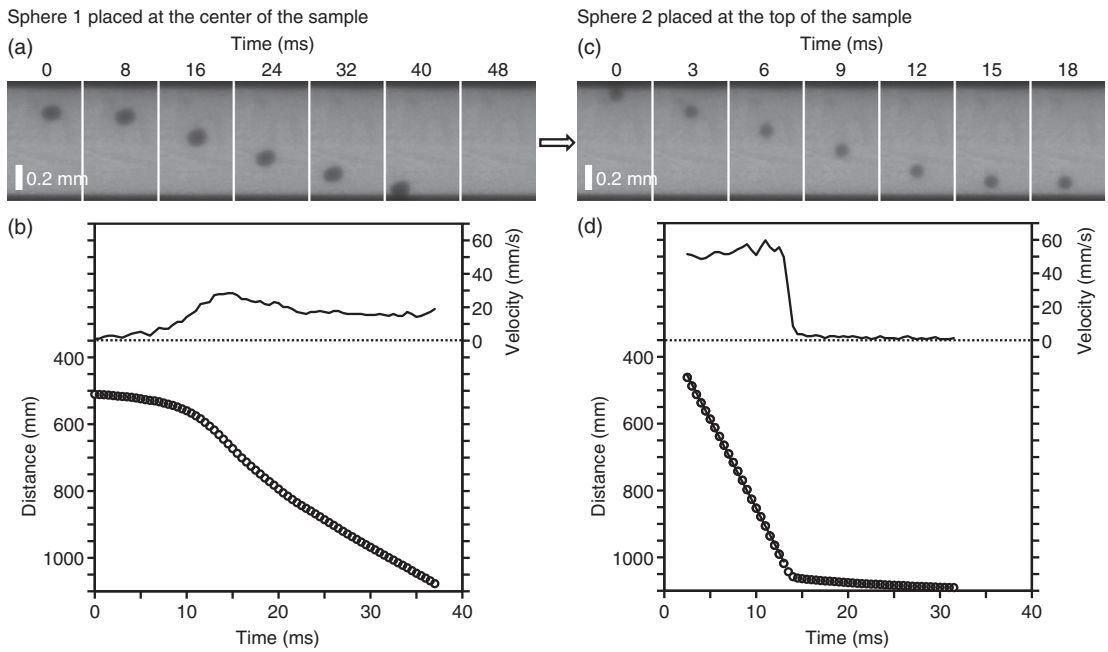


**Fig. 17.** X-ray radiography images of falling Pt sphere 1 (placed at the center of the sample) (a) and sphere 2 (placed at the top of the sample) (c), and the results of the falling distance analysis for sphere 1 (b) and for sphere 2 (d), respectively.

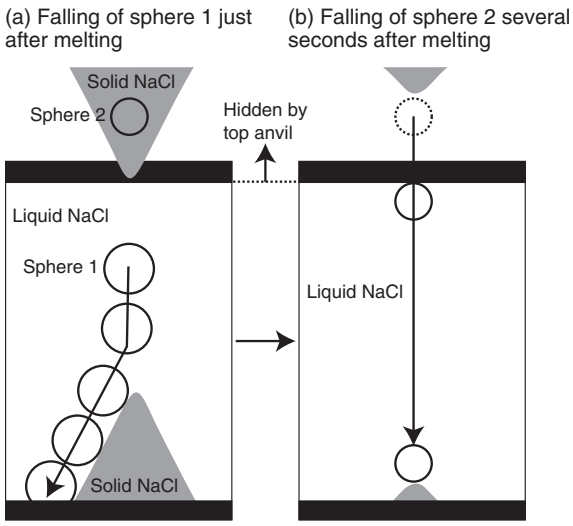


**Fig. 18.** Schematic illustrations of the motion of falling sphere 1 and 2, and probable sample conditions just after melting (a) and several seconds after melting.

to avoid uncertainty of incomplete melting of sample. However, even though sample is completely molten, it is important to confirm terminal velocity particularly for the viscosity measurement of low viscous liquids, because it is possible to take time to reach terminal velocity.

A previous study of Urakawa et al. (2001) showed estimation of time and distance required to reach terminal velocity using the following equations, which were derived from Stokes' equation:

$$v(t) = (v_0 - v_T)\exp\left(-\frac{g(\rho_l - \rho_s)}{v_T - \rho_s}t\right) + v_T, \quad (12)$$

$$D(t) = -\frac{(v_0 - v_T)v_T\rho_s}{g(\rho_l - \rho_s)}\left(\exp\left(-\frac{g(\rho_l - \rho_s)}{v_T\rho_s}t\right) - 1\right) + v_T t \quad (13)$$

These equation represents change of falling sphere velocity ($v$) with time ($t$) from initial velocity ($v_0 = 0$) to terminal velocity ($v_T$) and the resultant falling distance ($D$). Urakawa et al. (2001) calculated time and distance to reach terminal velocity by assuming $\rho_l = 6$ g/cm$^3$, $\rho_s = 20$ g/cm$^3$, $v_T = -3.81$ mm/s for simulating falling of 50 μm ball in liquid Fe–FeS having viscosity of 20 mPa s. The calculation yielded the time and distance to reach terminal velocity of 9 ms and 36 μm, respectively, and they concluded that these are short enough for their measurement on viscosity of liquid Fe–FeS.

It is more important to check falling velocity evolution with time in low viscous liquids, which yields high terminal velocity. We calculated the time and distance to reach terminal velocity using the Eqs. (12) and (13) by using the parameters of $\rho_l = 1.55$ g/cm$^3$, $\rho_s = 22.16$ g/cm$^3$, $v_T = -52.87$ mm/s for simulating falling of 106 μm ball in liquid NaCl having viscosity of 1.9 mPa s, corresponding to the experiment shown in Fig. 17c and d. Fig. 19 shows the calculated result of change of velocity and falling distance with time. The data clearly show that behavior of falling sphere in very low viscous liquids (such as liquid NaCl) is significantly different from those of ~10 times higher viscosity liquids simulated in Urakawa et al. (2001). Our calculation for low viscosity liquid showed higher slope in the velocity–time curve than that of Urakawa et al. (2001), which implies that speed to reach terminal velocity in low viscosity liquid is faster than that of higher viscosity liquid. However, final terminal velocity value of our calculation is ~14 times higher than that of Urakawa et al. (2001). As a result, the time to reach terminal velocity became longer than that of higher viscosity liquid of Urakawa et al. (2001). Our result shows more than 20 ms is required for reaching falling velocity close to the terminal velocity. As a result, more than 0.7 mm distance is needed to reach terminal velocity. Since the simple calculation of the Eqs. (12) and (13) does not include wall and end effect corrections, it is difficult to determine conclusive value of the time and distance required to reach terminal velocity. However, the analysis suggests that the time and distance to reach terminal velocity is not negligibly short in the viscosity measurement of low viscous liquids, and it is essential to monitor falling velocity change with time to confirm terminal velocity.

Author's personal copy



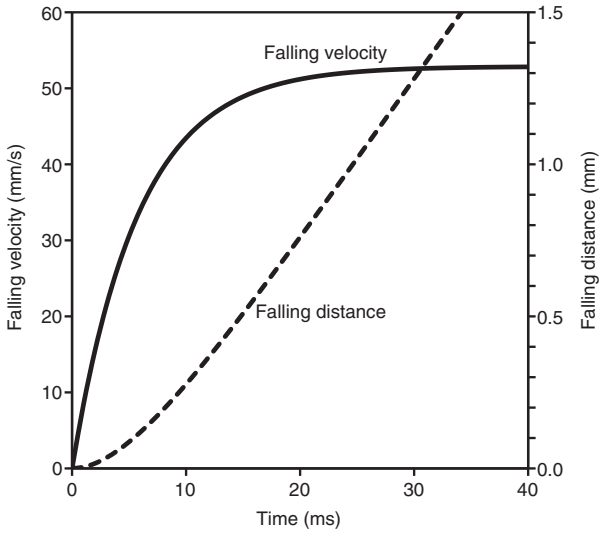


**Fig. 19.** Evolution of falling velocity with time and the resultant falling distance calculated by Eqs. (12) and (13), respectively.

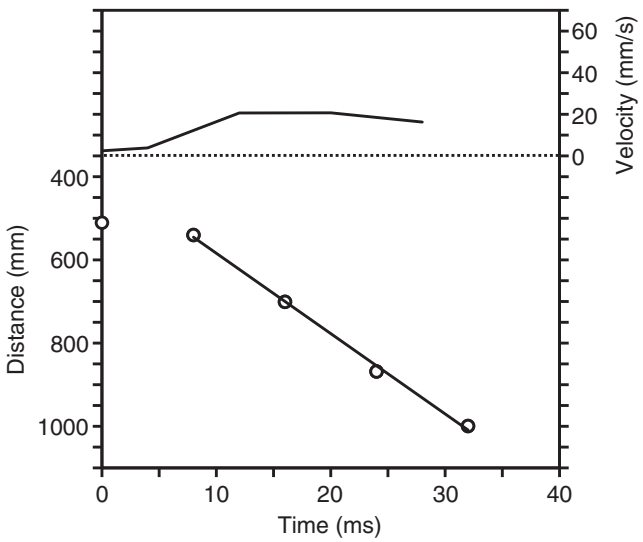


**Fig. 20.** A simulated result of falling of sphere 1 by 125 fps frame rate.

It may be difficult to clarify motion of falling sphere only with small numbers of images. Fig. 20 shows an example of analytical result for the falling of sphere 1 with reduced frame rate of 125 fps, which is the fastest frame rate used in previous high-pressure viscosity measurements. The falling of sphere 1 analyzed with 125 fps shows beautiful linear relationship between falling distance and time. Then, we may misinterpret that terminal velocity was achieved even for the falling of sphere 1 if we use the low frame rate measurement. However, our high-speed X-ray radiography has revealed that the falling of sphere 1 showed non-linear behavior in the falling distance with time (Fig. 17b). Thus, small number of sampling of falling sphere images may cause misunderstanding of terminal velocity, and it is important to observe falling sphere images with substantial oversampling to understand motion of falling sphere.

## 8. Concluding remarks

We have developed an integrated setup for multi-angle energy dispersive X-ray diffraction, ultrasonic measurement, and falling sphere viscometer using a Paris–Edinburgh press at sector 16-BM-B, HPCAT, at the APS, for comprehensively studying structures and physical properties of liquids and amorphous materials at high pressures and high temperatures. The liquid structure measurement by multi-angle energy dispersive X-ray diffraction can be combined with the elastic wave velocity or falling sphere viscosity measurement. The integrated capability opens a new way to investigate the direct link between microscopic structure and macroscopic physical properties of liquids and amorphous materials at high pressure and high temperature conditions. Knowledge of the correlation will be important for modeling liquid properties at high pressures and high temperatures, and thus for understanding the magmatic nature and the dynamics of the Earth's interior.

## Acknowledgments

We acknowledge Akihiro Yamada, Toru Inoue, Tony Yu, Tatsuya Sakamaki, and Zhicheng Jing for their helps in the developments of the Paris–Edinburgh cell experiments, and Lin Wang, Wenge Yang, and two anonymous reviewers for their review. This study was carried out at the Sector 16-BM-B, HPCAT at the Advanced Photon Source. HPCAT operations are supported by DOE-NNSA under Award No. DE-NA0001974 and DOE-BES under Award No. DE-FG02-99ER45775, with partial instrumentation funding by NSF. APS is supported by DOE-BES, under Contract No. DE-AC02-06CH11357. The Paris–Edinburgh cell program is partly supported by COMPRES. Y.W. acknowledges NSF Grant EAR-1214376.

## References

Besson, J.M., Nelmes, R.J., Hamel, G., Loveday, J.S., Weill, G., Hull, S., 1992. Neutron powder diffraction above 10 GPa. Phys. B: Condens. Matter 180–181 (Part 2), 907–910.
Brizard, M., Megharfi, M., Verdier, C., 2005. Absolute falling-ball viscometer: evaluation of measurement uncertainty. Metrologia 42, 298–303.
Cromer, D.T., 1969. Compton scattering factors for aspherical free atoms. J. Chem. Phys. 50, 4857–4859.
Cromer, D.T., Mann, J.B., 1967. Compton scattering factors for spherically symmetric free atoms. J. Chem. Phys. 47, 1892–1893.
Decremps, F., Belliard, L., Couzinet, B., Vincent, S., Munsch, P., Le Marchand, G., Perrin, B., 2009. Liquid mercury sound velocity measurements under high pressure and high temperature by picosecond acoustics in a diamond anvils cell. Rev. Sci. Instrum. 80, 073902–073903.
Dobson, D.P., Crichton, W.A., Vocadlo, L., Jones, A.P., Wang, Y., Uchida, T., Rivers, M., Sutton, S., Brodholt, J.P., 2000. In situ measurement of viscosity of liquids in the Fe–FeS system at high pressures and temperatures. Am. Mineral. 85, 1838–1842.
Egami, T., 1978. Structural relaxation in amorphous Fe40Ni40P14 B6 studied by energy dispersive X-ray diffraction. J. Mater. Sci. 13, 2587–2599.
Eggert, J.H., Weck, G., Loubeyre, P., Mezouar, M., 2002. Quantitative structure factor and density measurements of high-pressure fluids in diamond anvil cells by X-ray diffraction: argon and water. Phys. Rev. B 65, 174105.
Faxén, H., 1922. Der Widerstand gegen die Bewegung einer starren Kugel in einer zähen Flüssigkeit, die zwischen zwei parallelen ebenen Wänden eingeschlossen ist. Ann. Phys. 373, 89–119.
Gotou, H., Yagi, T., Okada, T., Iizuka, R., Kikegawa, T., 2011. A simple opposed-anvil apparatus for high pressure and temperature experiments above 10 GPa. High Press. Res. 31, 592–602.
Hosokawa, S., Matsuoka, T., Tamura, K., 1991. X-ray diffraction measurements for expanded liquid mercury in the metallic region. J. Phys.: Condens. Matter 3, 4443.
Kanzaki, M., Kurita, K., Fujii, T., Kato, T., Shimomura, O., Akimoto, S., 1987. A new technique to measure the viscosity and density of silicate melts at high pressures. In: Manghani, M.H., Shono, Y. (Eds.), High Pressure Research in Mineral Physics. Terrapub, Tokyo, pp. 195–200.
Kaplow, R., Strong, S.L., Averbach, B.L., 1965. Radial density functions for liquid mercury and lead. Phys. Rev. 138, A1336–A1345.
Katayama, Y., Tsuji, K., Shimomura, O., Kikegawa, T., Mezouar, M., Martinez-Garcia, D., Besson, J.M., Hausermann, D., Hanfland, M., 1998. Density measurements of liquid under high pressure and high temperature. J. Synchrotron Radiat. 5, 1023–1025.
Klotz, S., Hamel, G., Frelat, J., 2004. A new type of compact large-capacity press for neutron and X-ray scattering. High Press. Res. 24, 219–223.
Kono, Y., Irifune, T., Higo, Y., Inoue, T., Barnhoorn, A., 2010. P–V–T relation of MgO derived by simultaneous elastic wave velocity and in situ X-ray measurements: a new pressure scale for the mantle transition region. Phys. Earth Planet. Inter. 183, 196–211.

Author's personal copy



Kono, Y., Kenney-Benson, C., Park, C., Shen, G., Wang, Y., 2013. Anomaly in the viscosity of liquid KCl at high pressures. Phys. Rev. B 87, 024302.
Kono, Y., Park, C., Sakamaki, T., Kenny-Benson, C., Shen, G., Wang, Y., 2012. Simultaneous structure and elastic wave velocity measurement of $SiO_2$ glass at high pressures and high temperatures in a Paris–Edinburgh cell. Rev. Sci. Instrum. 83, 033905–033908.
Krisch, M., Loubeyre, P., Ruocco, G., Sette, F., Cunsolo, A., D'Astuto, M., LeToullec, R., Lorenzen, M., Mermet, A., Monaco, G., Verbeni, R., 2002. Pressure evolution of the high-frequency sound velocity in liquid water. Phys. Rev. Lett. 89, 125502.
Kushiro, I., Yoder Jr., H.S., Mysen, B.O., 1976. Viscosities of basalt and andesite melts at high pressures. J. Geophys. Res. 81, 6351–6356.
Liebske, C., Schmickler, B., Terasaki, H., Poe, B.T., Suzuki, A., Funakoshi, K.-i., Ando, R., Rubie, D.C., 2005. Viscosity of peridotite liquid up to 13 GPa: implications for magma ocean viscosities. Earth Planet. Sci. Lett. 240, 589–604.
Matsui, M., 2009. Temperature–pressure–volume equation of state of the B1 phase of sodium chloride. Phys. Earth Planet. Inter. 174, 93–97.
Maude, A.D., 1961. End effects in a falling-sphere viscometer. Br. J. Appl. Phys. 12, 293.
Mezouar, M., Faure, P., Crichton, W., Rambert, N., Sitaud, B., Bauchau, S., Blattmann, G., 2002. Multichannel collimator for structural investigation of liquids and amorphous materials at high pressures and temperatures. Rev. Sci. Instrum. 73, 3570–3574.
Morard, G., Mezouar, M., Rey, N., Poloni, R., Merlen, A., Le Floch, S., Toulemonde, P., Pascarelli, S., San-Miguel, A., Sanloup, C., 2007. Optimization of Paris–Edinburgh press cell assemblies for in situ monochromatic X-ray diffraction and X-ray absorption. High Press. Res. 27, 223–233.
Morard, G., Mezouar, M., Bauchau, S., Alvarez-Murqa, M., Hodeau, J.L., Garbarino, G., 2011. High efficiency multichannel collimator for structural studies of liquids and low-Z materials at high pressures and temperatures. Rev. Sci. Instrum. 82, 023904.
Nishida, K., Kono, Y., Terasaki, H., Takahashi, S., Ishii, M., Shimoyama, Y., Higo, Y., Funakoshi, K.-i., Irifune, T., Ohtani, E., 2013. Sound velocity measurements in liquid Fe–S at high pressure: implications for Earth's and lunar cores. Earth Planet. Sci. Lett. 362, 182–186.
Nishikawa, K., Iijima, T., 1984. Corrections for intensity data in energy-dispersive X-ray diffractometry of liquids. Application to carbon tetrachloride. Bull. Chem. Soc. Jpn. 57, 1750–1759.
Ohtani, E., Suzuki, A., Ando, R., Urakawa, S., Funakoshi, K., Katayama, Y., 2005. Viscosity and density measurements of melts and glasses at high pressure and temperature by using the multi-anvil apparatus and synchrotron X-ray radiation. In: Chen, J., Wang, Y., Duffy, T.S., Shen, G., Dobrzhinetskaya, L.F. (Eds.), Advances in High-Pressure Technology for Geophysical Applications. Elsevier, Amsterdam, pp. 195–210.
Perrillat, J.-P., Mezouar, M., Garbarino, G., Bauchau, S., 2010. In situ viscometry of high-pressure melts in the Paris–Edinburgh cell: application to liquid FeS. High Press. Res. 30, 415–423.
Sakamaki, T., Wang, Y., Park, C., Yu, T., Shen, G., 2012. Structure of jadeite melt at high pressures up to 4.9 GPa. J. Appl. Phys. 111, 112623.
Sharma, S.K., Virgo, D., Kushiro, I., 1979. Relationship between density, viscosity and structure of $GeO_2$ melts at low and high pressures. J. Non-Cryst. Solids 33, 235–248.
Shchennikov, V.V., Ovsyannikov, S.V., Bazhenov, A.V., 2008. A composite high-pressure cell with sintered diamond insets for study of thermoelectric and thermomagnetic properties in a range up to 30 GPa: application to Pr and PbTe. J. Phys. Chem. Solids 69, 2315–2324.
Shen, G., Sata, N., Newville, M., Rivers, M.L., Sutton, S.R., 2002. Molar volumes of molten indium at high pressures measured in a diamond anvil cell. Appl. Phys. Lett. 81, 1411–1413.
Shen, G., Prakapenka, V.B., Rivers, M.L., Sutton, S.R., 2004. Structure of liquid iron at pressures up to 58 GPa. Phys. Rev. Lett. 92, 185701.
Sugiyama, K., Shinkai, T., Waseda, Y., 1996. New ADXD/EDXD spectrometer for determining the structure of melts at high temperature. Sci. Rep. RITU A42, 231–237.
Terasaki, H., Kato, T., Urakawa, S., Funakoshi, K.-i., Suzuki, A., Okada, T., Maeda, M., Sato, J., Kubo, T., Kasai, S., 2001. The effect of temperature, pressure, and sulfur content on viscosity of the Fe–FeS melt. Earth Planet. Sci. Lett. 190, 93–101.
Terasaki, H., Suzuki, A., Ohtani, E., Nishida, K., Sakamaki, T., Funakoshi, K., 2006. Effect of pressure on the viscosity of Fe–S and Fe–C liquids up to 16 GPa. Geophys. Res. Lett. 33, L22307.
Tsuji, K., Yaoita, K., Imai, M., Shimomura, O., Kikegawa, T., 1989. Measurements of X-ray diffraction for liquid metals under high pressure. Rev. Sci. Instrum. 60, 2425–2428.
Urakawa, S., Terasaki, H., Funakoshi, K., Kato, T., Suzuki, A., 2001. Radiographic study on the viscosity of the Fe–FeS melts at the pressure of 5 to 7 GPa. Am. Mineral. 86, 578–582.
Waseda, Y., 1980. The Structure of Non-crystalline Materials: Liquids and Amorphous Solids. McGraw-Hill International Book Company.
Yamada, A., Wang, Y., Inoue, T., Yang, W., Park, C., Yu, T., Shen, G., 2011. High-pressure X-ray diffraction studies on the structure of liquid silicate using a Paris–Edinburgh type large volume press. Rev. Sci. Instrum. 82, 015103–015107.